Bone 48 (2011) 1388–1400

Contents lists available at ScienceDirect

Bone

journal homepage: www.elsevier.com/locate/bone

Impaired bone healing pattern in mice with ovariectomy-induced osteoporosis: A drill-hole defect model

Yi-Xin He [a], Ge Zhang [a,*], Xiao-Hua Pan [a,c], Zhong Liu [a], Li-zhen Zheng [a], Chun-Wai Chan [a], Kwong-Man Lee [d], Yong-Ping Cao [e], Gang Li [a], Lei Wei [f,g], Leung-Kim Hung [a], Kwok-Sui Leung [a,b], Ling Qin [a,b,*]

[a] Musculoskeletal Research Laboratory, Department of Orthopaedics and Traumatology, The Chinese University of Hong Kong, Shatin, Hong Kong, China
[b] Translational Medicine Research and Development Center, Institute of Biomedical and Health Engineering, Shenzhen Institute of Advanced Technology, Chinese Academy of Science, 518055 Shenzhen, China
[c] Department of Orthopedics, Second Hospital of Medical College of Ji Nan University, Shenzhen People's Hospital, 518020 Shenzhen, China
[d] Lee Hysan Clinical Research Laboratory, The Chinese University of Hong Kong, Shatin, Hong Kong, China
[e] Department of Orthopedics, Peking University First Hospital, 100034 Beijing, China
[f] Department of Orthopaedics, Warren Alpert Medical School of Brown University, Providence, RI, USA
[g] Department of Orthopaedics, The Second Hospital of Shanxi Medical University, Shanxi Key Lab of Bone and Soft Tissue Injury Repair. Taiyuan 030001, China

ARTICLE INFO

Article history:
Received 10 August 2010
Revised 4 March 2011
Accepted 14 March 2011
Available online 21 March 2011

Edited by: Harry Genant

Keywords:
Osteoporosis
Drill-hole
Micro-CT
Mouse
Bone healing

ABSTRACT

Objective: To establish a drill-hole defect model in osteoporotic mouse femur by comparing temporal cortical bone healing pattern between OVX-induced osteoporotic bone and sham-operated bone.
Methods: 3-month-old female C57BL/6 mice were randomly divided into an ovariectomy group (OVX) and a sham-operated group (Sham). At 6 weeks post-surgery, 7 mice from each group were sacrificed to examine the distal femur and femoral shaft by both micro-CT and mechanical testing for confirming established osteoporosis induced by OVX. In the remaining mice, a cortical bone defect 0.8 mm in diameter was created on the mid-diaphysis of the right femur. The local repair process at days 0, 3, 7, 10, 14 and 21 after creation of the drill-hole was *in vivo* monitored by high-resolution micro-CT scanning. At each time point, each animal was scanned four times and was removed from the scanner between scans to determine reproducibility. Mice were sacrificed at each time point ($n = 12$ at days 0, 3, 7, 10 and 14; $n = 20$ at day 21). Before sacrifice, sera were collected to examine expression of bone formation marker P1NP (procollagen type I N-terminal propeptide) and bone resorption marker CTX (C-terminal telopeptide of type I collagen). After sacrifice, callus samples were collected and subjected to the following analyses: micro-CT-based angiography; histological examination; immunohistochemical staining to determine estrogen receptor expression; quantitative real-time PCR analysis of collagen type I, collagen type II, collagen type X, osteocalcin, tartrate-resistant acid phosphatase, estrogen receptor alpha (ER alpha) and estrogen receptor beta (ER beta) gene expression; and three-point mechanical testing.
Results: At 6 weeks post-surgery, OVX mice had significantly lower bone mass, impaired bone micro architecture and compromised mechanical properties compared to the Sham mice. *In vivo* micro-CT analysis revealed that the bone volume fraction in the defect region was significantly lower in the OVX group from day 10 to day 21 post-injury as compared to the Sham group, and was significantly lower in the intra-medulla region in the OVX group from day 7 to day 14 as compared to the Sham group, consistent with the histological data. Analysis of bone biochemical markers indicated that circulating P1NP levels normalized by baseline in the OVX mice were significantly lower than in the Sham mice from day 7 to day 10, and that temporal expression of circulating CTX levels normalized by baseline was also lower in the OVX mice as compared to the Sham mice. These results were consistent with quantitative real-time PCR analysis. ER alpha mRNA expression was significantly lower in the OVX mice, whereas ER beta mRNA expression was significantly higher in the OVX mice as compared to the Sham mice at all time points examined, consistent with immunohistochemical staining. The restoration of femoral mechanical property, determined based on ultimate load and energy-to-failure, was significantly lower in the OVX mice than in the Sham mice. In addition, *in vivo* micro-CT scanning for quantifying new bone formation in the defect site was highly reproducible in this model.

Abbreviations: Micro-CT, Micro-computed tomography.

* Corresponding authors at: Musculoskeletal Research Laboratory, Department of Orthopaedics and Traumatology, The Chinese University of Hong Kong, Shatin, Hong Kong, China. Fax: +852 26324618.
E-mail addresses: zhangge@ort.cuhk.edu.hk (G. Zhang), lingqin@cuhk.edu.hk (L. Qin).

8756-3282/$ – see front matter
doi:10.1016/j.bone.2011.03.720

Conclusion: The bone healing of the drill-hole defect was impaired in mice with OVX-induced osteoporosis. The present study provides a model to investigate the functional role of specific gene in osteoporotic bone healing and may facilitate development of novel therapeutic strategies for promoting osteoporotic bone healing.

Introduction

The mechanism of impaired bone healing in postmenopausal osteoporosis is unknown

Bone healing is a specialized postnatal repair process that recapitulates embryological skeletal development [1], which involves a well-characterized cascade of events, including three major stages [2–4], *i.e.* inflammation reaction, callus mineralization, and callus remodeling [4]. Several molecular mechanisms regarding the roles of pro-inflammatory cytokines, TGFß superfamily, metalloproteinases and angiogenic factors in normal bone healing have been well established [3,5–10]. To date, clinical and experimental studies have consistently demonstrated that bone healing in postmenopausal osteoporotic women and estrogen depletion-induced osteoporotic animals is remarkably delayed or impaired [11–22]. However, the molecular signaling events responsible for delayed or impaired bone healing in postmenopausal osteoporosis remain unclear.

Limitations in currently available mouse models of osteoporotic bone healing

The development of genetically modified mice in recent years has provided a powerful tool for investigating the functional role of specific genes involved in osteoporotic bone healing. It should be pointed out that currently established mouse models for osteoporotic bone healing [23,24] have been greatly challenged by the mechanical instability at points of fixation. The single axis internal fixation model was questioned because of its angular motion and the external fixation model was disputed because of its decreased holding power of the screws in osteoporotic bone [25]. Therefore, an osteoporotic bone healing model with mechanical stability is highly appreciated. On the other hand, mice are technically difficult to employ in generating reproducible bone healing due to the large variation induced by their small bone size. For analysis of small bone healing, high-resolution *in vivo* micro-CT monitoring is the method of choice because it provides highly accurate and reliable data. Unfortunately, this technique cannot be used in the mouse bone healing models described above because the metal stabilization devices interfere with micro-CT imaging. Accordingly, it is necessary to establish a highly reproducible mouse model without the mechanical instability and imaging interference associated with current mouse models for investigating osteoporotic bone healing *in vivo* via high resolution micro-CT scanning.

Creation of a drill-hole defect at the mid-diaphysis of the femur for in vivo monitoring of bone healing in mice with ovariectomy-induced osteoporosis

It has been shown that drilling a hole in bone which partially disrupts the cortex and marrow is a technically simple and highly reproducible method for creating a bone defect for normal mouse bone healing studies; this method dose not necessitate a stabilization device, does not result in a high incidence of post-surgery fractures, and does not disturb the normal walking activity of mice [26]. Clinically, bridging of the fracture site with cortices or cortical continuity is the most commonly reported criteria for radiographic assessment of fracture union at any injury location in osteoporotic patients, although most osteoporotic bone injury cases with disruption of both cortex and marrow result in complex and variable patterns of healing [27]. It is therefore necessary to establish a mouse model focusing on cortical healing in osteoporotic bone. To date, cortical perforations generated by the drill-hole method have been performed using the femur metaphysis [28], the femur epimetaphysis [29], the femur diaphysis [30], or the tibia diaphysis [31]. The complexity of the interaction between cortical bone and trabecular bone at the femur metaphysis, the lengthy period required for cortical healing at the femur epimetaphysis [26], and the technical difficulties associated with analysis of the tibia diaphysis led us to speculate that the femur diaphysis may be a preferred skeletal site to address specifically the molecular mechanisms of cortical healing in osteoporotic bone. Moreover, a drill-hole defect in the femur diaphysis does not require a metal fixation device because mechanical instability is not a concern; this would facilitate the employment of high resolution micro-CT to monitor the bone healing process *in vivo*. However, the precise kinetics and patterns of cortical regeneration in osteoporotic bone induced by ovariectomy (OVX) have not been thoroughly examined.

In the present study, we examined the differences in cortical bone repair patterns over time between mice with OVX-induced osteoporosis and sham-operated (Sham) mice. Micro-CT was employed for analysis of callus angiogenesis and mineralization; quantitative real-time PCR was employed for quantifying bone healing related gene expression at mRNA level; enzyme-linked immunosorbent assay (ELISA) was performed to evaluate systemic bone turnover biochemical markers at protein level; decalcified histology was used to describe callus histopathology features at tissue level, and three-point bending test was employed to measure callus mechanical properties at functional level. Moreover, the reproducibility of the *in vivo* micro-CT monitoring technique for examining cortical healing of a drill-hole defect in the femur at mid-diaphysis was determined. In addition, estrogen receptor expressions within callus were also evaluated by both immunohistochemistry and quantitative real-time PCR, because dysregulation of estrogen receptors could be involved in the underlying mechanism responsible for osteoporotic bone healing after estrogen depletion.

Materials and methods

Experimental animals

In total, 174 female C57BL/6 mice were obtained from the Laboratory Animal Services Center of the Chinese University of Hong Kong. They were housed and acclimatized at the research animal laboratory. The Animal Experimentation Ethics Committee of The Chinese University of Hong Kong approved the care and experimental protocol of this study (Ref. No.09/001/GRF).

Surgical protocol and experimental design

The mice were subjected to ovariectomy (OVX) or sham operation (Sham) at 3 months of age. At 6 weeks post-surgery, 7 mice from each group were euthanatized, and right intact femora were collected for micro-CT analysis and subsequently for mechanical testing to confirm the osteoporotic condition. Thereafter, the remaining mice were anesthetized by intraperitoneal injections of ketamine hydrochloride (100 mg/kg body weight) and xylazine (4 mg/kg body weight). A skin incision was made over the right lateral femoral aspect and blunt dissection of the quadriceps was performed to expose the femoral

diaphysis. Perforations 0.8 mm in diameter were then locally generated through the posterior and anterior cortices using a 21-gauge needle (Fig. 1A and B). Holes were rinsed by injection of saline to remove bone fragments from the cavity. The muscles were subsequently repositioned, and the skin was closed with suture. The local site of the drill-hole was monitored *in vivo* by micro-CT to assess the healing progress (n = 8 in each group); animals were scanned four times at each time point and were removed from the scanner between each scan to assess reproducibility, including determination of precision errors (PE) and intraclass correlation coefficients (ICC). According to previous research regarding cortical defect healing in normal mice, there was hematoma formation at day 3, there was new bone formation at day 7 and day 10, and the defect region underwent remodeling at day 14 and day 21. Therefore, the mice from OVX (n = 80) and Sham (n = 80) were sacrificed on days 0 (n = 12), 3 (n = 12), 7 (n = 12), 10 (n = 12), 14 (n = 12) and 21 (n = 20) post-injury. Before sacrifice, sera were collected via cardiac puncture and analyzed by ELISA for bone formation and bone resorption markers. Immediately after sacrifice, radiopaque contrast reagents (Microfil 117; Flow Tech, Carver, MA, USA) were perfused for micro-CT based angiography. Thereafter, femora samples from each group were collected for angiography (n = 4), histology or immunohistochemistry (n = 4), quantitative real-time PCR (n = 4), and mechanical testing (n = 8).

Micro-CT analysis of intact femur

Metaphysis region of the right distal femur and femoral shaft were scanned by micro-CT (vivaCT 40; SCANCO MEDICAL, Bassesdorf, Switzerland) with a source voltage of 70 keV, current of 114 μA and 10.5 μm isotropic resolution.

Distal femur scans were performed from the growth plate proximally to 2.2 mm. From this region, a series of slices starting at a distance of 0.5 mm proximal from the higher end of the growth plate with a length of 1.05 mm was chosen for the evaluation. The trabecular part of the femur was separated with semi-automatically drawn contours. The complete secondary spongiosa of the distal femur was evaluated, thereby avoiding sampling errors incurred by random deviations of a single section. The resulting gray-scale images were segmented using a low-pass filter to remove noise and a fixed threshold (sigma = 1.2, support = 2 and threshold = 190) to extract the mineralized bone phase. After 3D reconstruction, bone volume fraction (BV/TV), trabecular number (Tb.N), trabecular thickness (Tb.Th), trabecular separation (Tb.Sp), connectivity density (Conn.D), structural model index (SMI) and bone mineral density (BMD) were calculated using built-in software [32].

Femoral shaft scans were performed from 6 mm proximal of the distal femur and proceeded proximally in 10 μm sections, with a total of 105 sections per scan. The outer contour of the bone was automatically identified using the built-in Scanco iterative contouring tool (steepest edge finder). Threshold parameters (sigma = 1.2, support = 2 and threshold = 250) were used for segmenting a 2D image into bone and background. The total area (TA) was calculated by counting all voxels within the contour and in the bone area (BA) by counting all voxels that were segmented as bone. The marrow area (MA) was calculated as the difference between the TA and BA. This analysis was performed on the first 20 slices, using the average for the final calculation. The bone area fraction (BA/TA), cortical thickness (Ct.Th), polar moment of inertia (pMOI) and BMD were calculated using built-in software [33].

In vivo micro-CT analysis of new bone formation in the drill-hole site

Before scanning, mice were anesthetized and placed prone on a scan stage. A vivaCT 40 (Scanco Medical) was employed to scan a region of the femur 4 mm in length covering the drill-hole site at a voltage of 70 keV with a current of 114 μA. After automatic reconstruction, 2D slices with 19 μm isotropic resolution were generated and used to select the region of interest (ROI) for 3D reconstruction. For initial analysis, two square regions of interest (ROIs) encompassing the posterior and anterior cortical defects and another square ROI positioned in the intra-medullary space between the two defects were selected (Fig. 1C). After choosing a threshold (sigma = 1.2, support = 2 and threshold = 190), the bone volume fraction (BV/TV) was calculated using built-in software.

Micro-CT-based angiography

Micro-CT-based angiography was performed to evaluate vascularity [34]. The vasculature of each mouse was sequentially perfused at physiological pressure using heparinized (100 U/ml) normal saline, followed by 10% neutral-buffered formalin. The vascular system was injected with Microfil 117 (Flow Tech; Carver, MA), a radiopaque, lead chromate-based contrast reagent and allowed to polymerize for 24 h at 4 °C. The femora were isolated from the surrounding musculature,

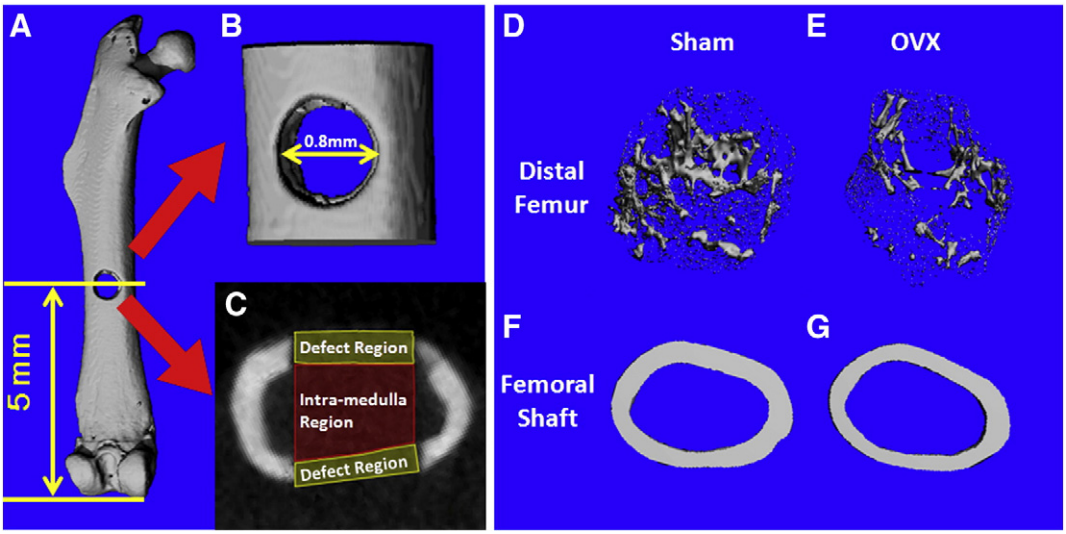

Fig. 1. Schematic representation of the drill-hole defect for comparison of bone structure between Sham and OVX mice using micro-CT analysis. (A and B) Dimensions and positioning of the drill-hole injury generated in the mid-diaphysis of the right femur. (C) Definition of the defect region and intra-medulla region in a representative two-dimensional image generated from micro-CT analysis. Representative 3D images of the metaphysic regions of the distal femur (D and E) and the femoral shaft regions (F and G) following micro-CT analysis of Sham and OVX mice are shown. Less trabecular bone and thinner cortical bone were observed in the OVX mice compared to the Sham mice and at 6 weeks post-surgery.

stored at 4 °C for 48 h in 10% neutral-buffered formalin, transferred to a 9% formic acid solution for 48 h to decalcify the mineralized bone, washed thoroughly using water, and stored in 10% neutral-buffered formalin until imaging. The specimens were imaged using a vivaCT 40 (Scanco Medical) with a voltage of 70 keV, a current of 114 μA and 10.5 μm isotropic resolution. The drill-hole site was selected as the volume of interest, and the 2D images were globally thresholded based on x-ray attenuation and used to construct the contrast-filled vascular network segmented from the surrounding tissues. The vessel volume fraction was calculated using built-in software [34,35].

Histological examination

Isolated femora were fixed in 10% neutral-buffered formalin, transferred to 70% ethanol, and decalcified in 9% formic acid. After tissue processing, the specimens were embedded in paraffin. Sections (5 μm) were cut sagittally along the femoral shaft axis and collected on glass slides, deparaffinized, and subjected to hematoxylin and eosin (H&E) staining using standard protocols and tartrate-resistant acid phosphatase (TRAP) staining using manufacturer's protocol (Sigma #387A; Sigma-Aldrich, St. Louis, USA.). After mounting with coverslips, the specimens were viewed and analyzed under a light microscope (Leica DMRB DAS; Leica, Heerbrugg, Switzerland).

Immunohistochemistry

To determine the localization of estrogen receptors in the defect site, sections were deparaffinized using xylene and rehydrated using graded series of alcohol concentrations. Endogenous peroxidase was quenched using 3% hydrogen peroxide for 10 min. Nonspecific binding of epitopes was blocked using 1:10 normal blocking serum. Slides were incubated at 4 °C overnight in a 1:100 dilution of mouse estrogen receptor (ER) alpha (sc-7207) or ER beta primary antibody (sc-8974; Santa Cruz Biotechnology, Santa Cruz, CA, USA.). Sections were washed and incubated with biotinylated secondary antibody (sc-7207; Santa Cruz Biotechnology,) for 30 min followed by incubation with peroxidase substrate for 10 min. The sections were washed and incubated in deionized water for 5 min, counterstained with H&E, and analyzed under a light microscope (Leica DMRB DAS) [36,37].

Quantitative real-time PCR

Callus samples were isolated from the defect sites. The samples were frozen in liquid nitrogen, pulverized using a Mikro-Dismembrator (Sartorius Stedim Biotech S.A., Aubagne Cedex, France), and total RNA was isolated using the RNeasy® Mini Kit (QIAGEN, Dusseldorf, Germany). The concentration of the total RNA was determined using a spectrophotometer. cDNA was synthesized from 0.5 μg of total RNA using a commercial first-strand cDNA synthesis kit (QIAGEN, Dusseldorf, Germany). Reverse transcription PCR was performed using primers specific for amplification of murine collagen type I (Col1a1), collagen type II (Col2a1), collagen type X (ColX), osteocalcin (OC), tartrate-resistant acid phosphatase (TRAP), ER alpha and ER beta [genes] (see Table 1 for specific primer sequences). Col1a1 is the major bone matrix protein; Col2a1 is maximally expressed during chondrocyte proliferation; ColX peaks during terminal differentiation of chondrocytes; osteocalcin is expressed in fully matured osteoblasts and TRAP is expressed by osteoclasts during the resorptive process. Real-time PCR reactions were performed using SYBR Green in a 7900HT Fast Real-Time PCR System (Applied Biosystems, Foster City, California, USA). All gene expression levels were normalized to β-actin [34].

Analysis of bone formation and resorption markers

Sera were assayed for circulating levels of procollagen type I N-terminal propeptide (PINP) (bone formation marker) and C-terminal telopeptide of type I collagen (CTX) (bone resorption marker) by ELISA (IDS Ltd., Boldon, UK) following the manufacturer's protocol. Briefly, 50 μl serum was added to a polyclonal rabbit anti-P1NP or anti-CTX coated plate in duplicate and incubated with 50 μl biotin-labeled P1NP or CTX for 1 h and then 150 μl avidin-linked horseradish peroxidase was added to each well and incubated for 30 min. Finally, 150 μl tetramethylbenzidine (TMB) substrate was added for color development, which was measured using a microplate reader within 30 min of adding stop solution. Standard curves were generated using serial dilutions of the P1NP or CTX calibration standards supplied in the ELISA kit [38]. The expression levels were normalized to baseline (day 0 serum).

Mechanical testing

The mechanical properties of the femurs with drill-hole defects were examined at 21 days post-surgery using a three-point bending test. The intact contralateral femur was also tested as an internal control. Before mechanical testing, the femur was taken out from the freezer and thawed overnight at air conditioned room temperature of 22 °C. A material test machine (H25KS; Hounsfield Test Equipment Ltd. UK) with a 25 N load cell was used to test the femur to failure. The femurs were positioned horizontally with the anterior surface upwards, centered on the supports with 10 mm apart. Load was applied at the drill-hole site constantly with displacement rate of 5 mm/min and directed vertically to mid-shaft with anterior surface upward. After failure, the load vs. displacement curves were recorded. The ultimate load (UL) and the energy-to-failure were calculated using built-in software (QMAT Professional; Tinius Olsen, Inc. Horsham, PA, USA). The relative UL and energy-to-failure of the femur with the drill-hole was normalized to those of the intact femur. Intact femurs harvested from the both Sham and OVX mice 6 weeks post-surgery were evaluated by the same protocol [33].

Statistical analysis

Precision errors (PEs) were defined to best characterize the reproducibility of a given bone measurement technique [39]. In that approach, the short-term precision of an individual subject (SD_j) was defined as the standard deviation of *n* repeated measurement on a given

Table 1
Oligonucleotide primer sequences for real-time PCR analysis of gene expression.

Target gene	Forward primer	Reverse primer
β-actin	5′-AGATGTGGATCAGCAAGCAG-3′	5′-GCGCAAGTTAGGTTTTGTCA-3′
Col1a1	5′-ACGTCCTGGTGAAGTTGGTC-3′	5′-CAGGGAAGCCTCTTTCTCCT-3′
Col2a1	5′-ACTGGTAAGTGGGGCAAGAC-3′	5′-CCACACCAAATTCCTGTTCA-3′
ColX	5′-ACCCCAAGGACCTAAAGGAA-3′	5′-CCCCAGGATACCCTGTTTTT-3′
Osteocalcin	5′-GCAGGAGGGCAATAAGGT-3′	5′-CGTAGATGCGTTTGTAGGC-3′
TRAP	5′-CAGCCCAAAATGCCTCGA-3′	5′-GCTTTTTGAGCCAGGACAGC-3′
ER alpha	5′-TCTGCCAAGGAGACTCGCTACTGT-3′	5′-GCTTGGCCAAAGGTTGGCAG-3′
ER beta	5′-GCCAACCTCCTGATGCTTCTTT-3′	5′-TTGTACCCTCGAAGCGTGTGA-3′

subject *j*. PEs may be expressed as the coefficient of variation ($\%CV_j$) of repeated measurements given on a percentage basis:

$$\%CVj = \frac{SD_j}{\overline{X}_j} \cdot 100\% \quad (1)$$

The precision error (PE_{SD}) (Eq. (2)) and percent precision error ($PE_{\%CV}$) (Eq. (3)) were calculated for each group for each time point by determining the root mean square average of the standard deviations (SD_j) and coefficients of variation (CV_j), respectively, established by Eq. (1) for *m* subjects:

$$PE_{SD} = \sqrt{\sum_{j=1}^{m} SD_j^2 / m} \quad (2)$$

$$PE_{\%CV} = \sqrt{\sum_{j=1}^{m} \%CV_j^2 / m} \quad (3)$$

Confidence intervals (CI) were also determined for all of the $PE_{\%CV}$ values using a χ^2 distribution where *df* represents the total degrees of freedom (m(n − 1)).

$$\frac{df}{\chi 1-\frac{\alpha}{2},df} PE_{\%CV^2} < \sigma^2 < \frac{df}{\chi \frac{\alpha}{2},df} PE_{\%CV^2} \quad (4)$$

Intraclass correlation coefficients (ICC) and their 95% CIs were also calculated to determine reproducibility [40]. The ICC was the ratio of the variance within subjects over the sum of the variances plus error. This corresponds to the ICC (3,1) model as described by Shrout and Fleiss [40], where the values vary between 0 and 1, with 1 representing perfect reproducibility.

$$ICC = \frac{F_0 - 1}{F_0 + (n-1)} \quad (5)$$

F_0 represents the ratio between subject mean squares over the residual within-subject mean squares and *n* represents the number of measurements (current study, $n = 4$). We then calculated the ICC and their 95% CIs again.

Data were expressed as the means ± SD. Data from repeated micro-CT measurements were analyzed by repeat measure analysis of variance (ANOVA) comparing the subgroups (Sham and OVX) at the various follow up times (0, 3, 7, 10, 14, and 21 days post-injury). Data from non-repeated measurements, including determination of mRNA expression and sera biomarker concentrations were analyzed by two-way ANOVA with a Tukey post-hoc test, and mechanical testing data were analyzed by Student's *t*-test. All statistical analyses were performed using SPSS software, version 16.0 (SPSS, Chicago, IL). *P* values less than 0.05 were considered significant.

Results

Confirmation of osteoporotic bone prior to generation of a drill-hole defect

Micro-CT 3D images revealed that OVX mice had less trabecular bone, disorganized trabecular architecture, expanded marrow cavities and thinning cortical bones compared to the Sham mice (Fig. 1D–G). The BV/TV, Tb.N, Conn.D and BMD in the distal femur were significantly lower in OVX mice than in Sham mice, whereas the Tb.Sp was significantly higher in OVX than in Sham mice. The BA, BA/TA, Ct.Th, pMOI, and BMD in the femoral shaft were also significantly lower in OVX mice than in Sham mice (Table 2). In addition, the ultimate load and energy-to-failure were also compromised in the OVX mice as compared to the Sham mice (Table 2).

Table 2
Micro-CT analysis and mechanical testing of intact femurs from OVX and Sham mice at 6 weeks post ovary surgery.

	OVX	Sham
Micro-CT analysis of distal femur		
BV/TV (%)	1.91 ± 0.94*	3.33 ± 1.31
Tb.N (mm^{-1})	2.03 ± 0.22*	2.93 ± 0.4
Tb.Th (mm)	0.04 ± 0.01	0.04 ± 0.01
Tb.Sp (mm)	0.50 ± 0.05*	0.34 ± 0.05
Conn.D (mm^{-3})	6.90 ± 3.2*	17.50 ± 7.2
SMI (−)	3.71 ± 0.61	3.44 ± 0.44
BMD (mg HA/cm^3)	18.50 ± 14.1*	42.40 ± 12.3
Micro-CT analysis of femoral shaft		
TA (mm^2)	1.63 ± 0.09	1.63 ± 0.06
BA (mm^2)	0.67 ± 0.03*	0.72 ± 0.04
MA (mm^2)	0.96 ± 0.06	0.92 ± 0.05
BA/TA (%)	41.20 ± 1.13*	43.80 ± 1.64
Ct.Th (mm)	0.16 ± 0.01*	0.18 ± 0.01
pMOI (mm^4)	0.28 ± 0.03*	0.32 ± 0.02
BMD (mg HA/cm^3)	426.00 ± 17*	453.00 ± 26
Mechanical testing of femoral shaft		
Ultimate load (N)	15.20 ± 1.96*	18.50 ± 0.57
Energy-to-failure (mJ)	3.40 ± 0.4*	4.20 ± 0.7

N = 7.
* P < 0.05 for significant difference between the OVX and Sham groups.

General observation of mice following drill-hole surgery

After the drill-hole surgeries, no mortality or femoral fractures were recorded throughout the study. All mice were able to walk normally 18 h after surgery.

In vivo micro-CT analysis of new bone in the drill-hole site of mouse femurs

In OVX and Sham groups, modestly mineralized calluses appeared at both the defect region and intra-medulla region 7 days after drill-hole surgery. At day 10, the extent of callus mineralization had increased, the intra-medulla region was predominantly occupied by mineralized callus, and the defect region was partially bridged. At day 14, the mineralized callus within the intra-medulla region was remodeled and the defect region was completely bridged. However, the extent of callus mineralization and the volume of mineralized callus was lower in the OVX group than the Sham group from day 7 to day 10; remodeling of newly formed bone at the cortical bone gap was greater in the Sham group than in the OVX group from day 14 to day 21(Fig. 2A and B).

Changes in the BV/TV over time in the drill-hole sites were significantly different between the OVX group and the Sham group. In both groups, the BV/TV in the defect region moderately increased from day 0 to day 7, substantially increased after day 7, peaked at day 14, and then decreased from day 14 to day 21. Compared to the Sham group, the BV/TV was significantly lower in the OVX group from day 10 to day 21 (Fig. 2C). In both groups, the BV/TV in the intra-medulla space moderately increased from day 0 to day 3, substantially increased from day 3, peaked at day 10, and returned to baseline at day 21. The BV/TV was significantly lower in the OVX group as compared to the Sham group from day 7 to day 14 (Fig. 2D).

In vivo micro-CT analysis of new bone in drill-hole sites is highly reproducible

The $PE_{\%CV}$ for micro-CT analysis of the defect region ranged from 1.87% (day 14) to 3.39% (day 7), and the $PE_{\%CV}$ for micro-CT analysis of the intra-medulla region ranged from 1.95% (day 14) to 3.36% (day 3). The mean bone volume fraction, PE_{SD}, $PE_{\%CV}$, and 95% CIs are given in Table 3. The ICC for micro-CT analysis of the defect region ranged from 0.956 (day 14) to 0.993 (day 3), and the ICC for micro-CT analysis of

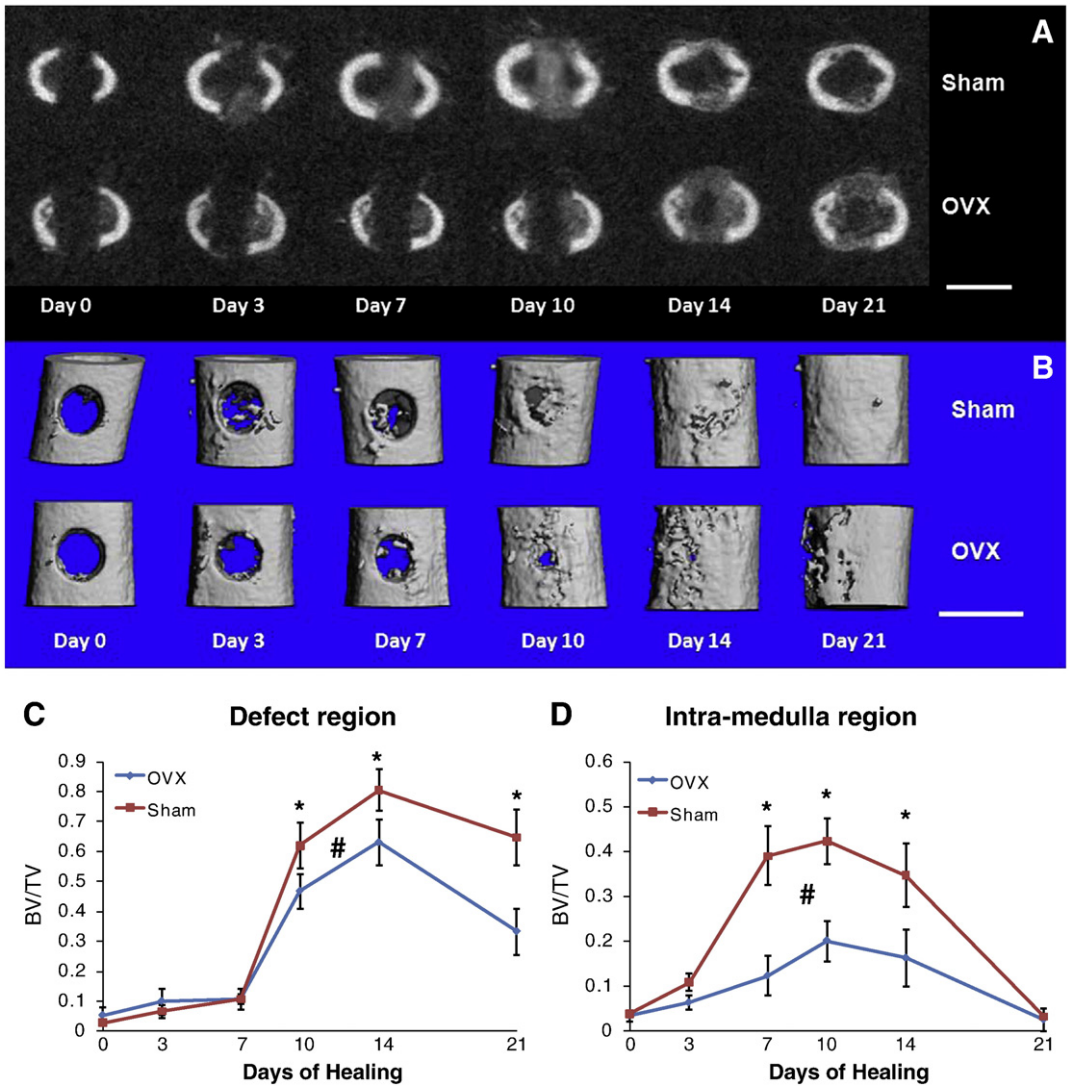

Fig. 2. Temporal micro-CT analysis of bone healing. Representative 2D (A) and 3D (B) images generated from micro-CT analysis of bone healing in Sham and OVX mice following drill-hole surgery (the same animal leg was used for each longitudinal series). Scale bar, 1 mm. (C) Quantification of new bone volume fraction in the defect region. (D) Quantification of new bone volume fraction in the intra-medullar region. N = 8 for each group, #: $P<0.05$ for comparison between Sham curve and OVX curve by repeat measure ANOVA; *: $P<0.05$ for comparison between Sham and OVX at same time point by Tukey post hoc test.

the intra-medulla region ranged from 0.967 (day 21) to 0.994 (day 14). ICC values and their corresponding 95% CIs are also shown in Table 3.

Micro-CT angiography

Three-dimensional angiograms generated from micro-CT analysis of mouse femurs following drill-hole surgery indicated that the number of the vessel-like structures was lower in OVX mice than in Sham mice, and the network of the vessel-like structures was poorly connected in the OVX group compared to the Sham group at day 7 (Fig. 3A and B). Quantification of angiograms indicated that the volume of vessel-like structures in OVX mice was lower than those in Sham mice at both day 3 and day 7 (Fig. 3C and D).

Histological observation of bone healing

At day 3 after drill-hole surgery, there was a predominance of soft tissue reaction composed of a mixture of hematoma and granulation tissue in both OVX and Sham groups. More vessel-like structures penetrating into the drill-hole site from the adjacent marrow were observed in the Sham mice as compared to the OVX mice. At day 7, newly woven bone was identified across the intra-medulla region and cortical gap; however, the volume of these bony structures was lower in the OVX mice compared to the Sham mice. At day 10, spicules of woven bone completely filled the intra-medulla region and partially bridged the cortical gap. The spicules of woven bone were thicker and denser in the Sham mice compared to the OVX mice. More TRAP-positive cells were observed in the Sham mice when compared to the OVX mice (Fig. 4C and D), which indicated more osteoclast activities in the Sham mice. At day 14, woven bone in the intra-medulla region was largely absent in the Sham mice, whereas it persisted in the OVX mice. The cortical gap was completely bridged by dense woven bone in the Sham mice, but was bridged by loose woven bone in the OVX mice. At day 21, the woven bone in the intra-medulla region had decreased to a level comparable with intact bone in the Sham mice, whereas residual woven bone remained in the intra-medulla region in the OVX mice. The cortical gap could not be identified in the Sham mice, whereas it was visible in the OVX mice, as indicated by the presence of some woven bone and increased porosity within the cortex (Fig. 4A and B). Generally, little cartilaginous tissue was visible in the drill-hole site during the healing process in both OVX and Sham groups.

Table 3
Reproducibility of *in vivo* bone volume fraction measurement in new bone using micro-CT analysis of the drill-hole site.

Region	Parameter	Days post drill-hole surgery					
		0	3	7	10	14	21
Defect region	Mean	0.0284	0.0669	0.1067	0.6203	0.8051	0.6471
	PESD	0.0010	0.0020	0.0036	0.0128	0.0149	0.0146
	PE%CV	3.31%	3.10%	3.39%	2.09%	1.87%	2.30%
	95%CI low	2.58%	2.42%	2.65%	1.63%	1.46%	1.79%
	95%CI high	4.60%	4.32%	4.71%	2.91%	2.60%	3.20%
	ICC	0.987	0.993	0.958	0.971	0.956	0.981
	95%CI low	0.964	0.978	0.883	0.919	0.876	0.944
	95%CI high	0.997	0.998	0.990	0.993	0.990	0.996
Intra-medulla region	Mean	0.0388	0.1085	0.3901	0.4234	0.3472	0.0325
	PESD	0.0010	0.0034	0.0081	0.0093	0.0067	0.0008
	PE%CV	2.70%	3.36%	2.08%	2.25%	1.95%	2.30%
	95%CI low	2.11%	2.62%	1.62%	1.75%	1.52%	1.80%
	95%CI high	3.76%	4.67%	2.89%	3.12%	2.71%	3.20%
	ICC	0.980	0.968	0.993	0.977	0.994	0.967
	95%CI low	0.943	0.908	0.981	0.933	0.984	0.906
	95%CI high	0.995	0.993	0.999	0.995	0.999	0.992

PE, precision error; SD, standard deviation; CV, coefficient of variation; CI, confidence interval and ICC, intraclass correlation coefficient (ICC).

Immunohistochemical analysis of ER alpha and beta expression during bone healing

During the entire healing period, the immunoreactive signal for ER alpha in callus tissue taken from the drill-hole site was weaker in the OVX mice than in the Sham mice, whereas the signal for ER beta was stronger in the OVX mice as compared to the Sham mice (Fig. 4C–F).

Quantitative real-time PCR analysis of gene expression during bone healing

In Sham and OVX mice, the mRNA expression levels of Col1a1 and osteocalcin steadily increased from day 0, peaked at day 7, and then decreased from day 7 to day 21. Col1a1 and osteocalcin mRNA expression levels were significantly higher in the Sham mice than in the OVX mice at day 7 and day 10 after drill-hole surgery (Fig. 5A and D). Col2a1 and Col10a1 mRNA expression levels were low at all time points, and there was no difference between the OVX and Sham mice (Fig. 5B and C). The mRNA expression levels of TRAP in both groups steadily increased from day 3 to day 10 and decreased thereafter, and TRAP mRNA levels were significantly lower in the OVX mice as compared to the Sham mice at day 10 and day 14 (Fig. 5E). At all time points, ER alpha mRNA expression levels were significantly lower in the OVX mice compared to the Sham mice (Fig. 5F), whereas ER beta mRNA expression levels were significantly higher in the OVX mice compared to the Sham mice (Fig. 5G).

Analysis of bone formation and resorption markers during bone healing

Circulating P1NP levels steadily increased from day 3, peaked at day 10, and then decreased from day 10 to day 21 in the Sham mice, whereas the levels peaked at day 14 and decreased thereafter in the OVX mice (Fig. 5H). At day 7 and day 10, circulating P1NP levels in the Sham mice were significantly higher than in the OVX mice. The circulating CTX levels in the both groups steadily increased from day 3 to day 14 and decreased thereafter and were significantly lower in the OVX mice as compared to the Sham mice at day 10 and day 14 (Fig. 5I).

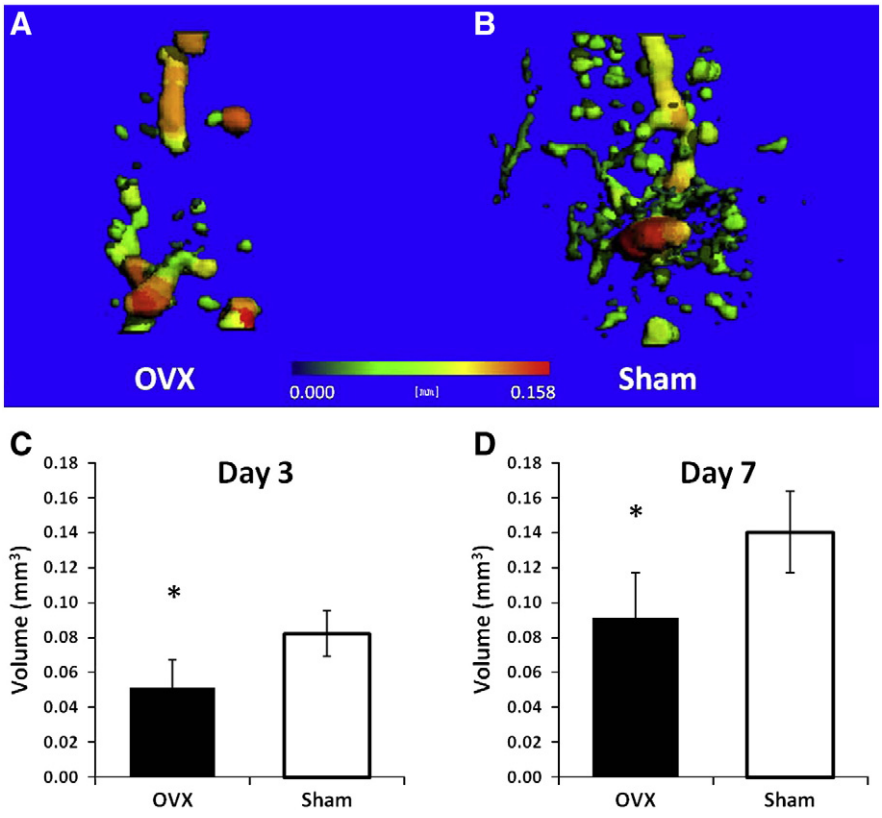

Fig. 3. Analysis of the volume of vessel-like structures in drill-hole sites. (A and B) Representative 3D angiographs comparing the vessel-like structures in the drill-hole sites at day 7 post-injury between OVX and Sham mice, respectively, are shown. The color indicates the thickness (mm) of the vessel-like structures. (C) Quantification of the volume of vessel-like structures at day 3. (D) Quantification of the volume of vessel-like structures day 7. N = 4 for each group, *: $P<0.05$ between the Sham and OVX groups.

Mechanical testing of femurs from Sham and OVX mice

At day 21 post drill-hole surgery, the ultimate load and energy-to-failure of femurs from the Sham mice recovered to 85% and 77% of that from intact femurs, respectively, whereas the ultimate load and energy-to-failure in the OVX mice only recovered to 68% and 55% of that from intact femurs, respectively. The restoration of ultimate load and energy-to-failure of femurs were significantly lower in the OVX mice than in the Sham mice (Fig. 6A and B).

Discussion

In this study, we compared for the first time the temporal and spatial changes of bone healing in drill-hole defect between Sham-operated control mice and OVX-induced osteoporotic mice, and established an osteoporotic mouse bone healing model with dominant intramembranous ossification. It was demonstrated that osteoporotic bone healing was impaired in neovascularization, osteogenesis, remodeling and mechanical properties. Moreover, the estrogen receptors expressions were dysregulated in OVX mice, and it could contribute to the underlying mechanism of the impaired healing. In addition, *in vivo* micro-CT technology showed high reproducibility in monitoring bone healing in the mice model.

Bone healing with dominant intramembranous ossification

In this model, a unilateral perforation 0.8 mm in diameter was generated in the femoral cortex at midshaft. The lesions did not necessitate stabilization devices, did not result in a high incidence of fracture, and did not disturb the normal walking activity of mice. Histological evidence demonstrated that very little cartilage accumulation was observed within the regenerating zone at any period following drill-hole surgery in both Sham and OVX groups. Consistently, molecular evidence also showed that the chondrocyte-related genes *col2a1* (which are maximally expressed during chondrocyte proliferation) and *col10a1* (which peak during chondrocyte terminal differentiation) remained low throughout the study period in both groups. Unlike most other fracture models with mechanical instability [41], the absence of a cartilaginous template in the healing process was dominant in our model with mechanical stability; this has also been demonstrated in other studies using drill-hole defect models [26,31,42,43]. This indicated that the characteristics of bone healing in this model were intramembranous ossification dominant.

Impaired osteoporotic bone healing

Impaired neovascularization

Angiogenesis is an essential stage during bone healing, and previous studies demonstrated that angiogenic factors, such as vascular endothelial

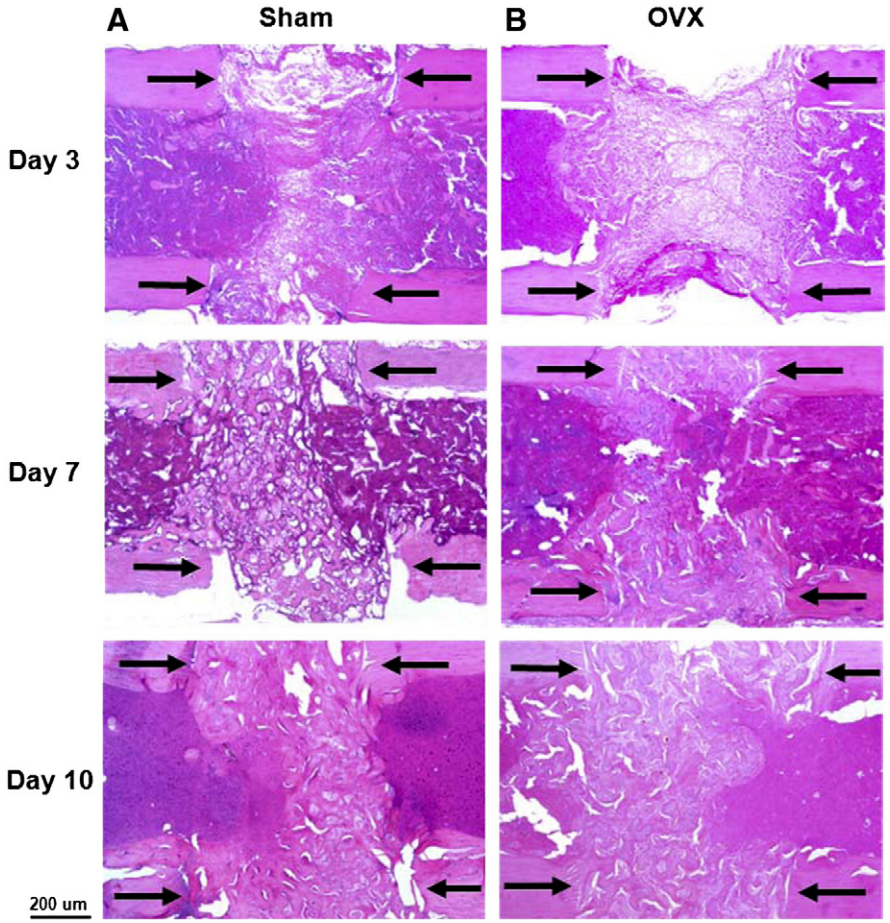

Fig. 4. Histological and immunohistochemical analysis of the progression of bone healing and ER expression in Sham and OVX mice. Representative photomicrographs of callus sections from the Sham and OVX groups demonstrate bone healing following drill-hole surgery. (A and B) Callus sections taken on the indicated day post-surgery were stained with H&E, and images were acquired at 100× magnification. Arrows indicate cortical gaps. (C and D) Callus sections taken on day 10 post-surgery were stained with TRAP, and images were acquired at 400× magnification. Arrows indicate TRAP-positive cells and dotted arrows indicate trabecular surface. More TRAP-positive cells were observed in the Sham mice callus compared to the OVX mice callus. (E–H) Callus sections taken on day 10 post-surgery were subjected to immunohistochemical staining using anti-ER alpha (E and F) or anti-ER beta (G and H). Arrowheads indicate positive signals. Strong ER alpha expression (E) but weak ER beta expression (G) was observed in the Sham mice callus, whereas weak ER alpha expression (F) but strong ER beta expression (H) was observed in the OVX mice callus. Similar patterns of ER alpha and ER beta expression were observed at other time points (data not shown).

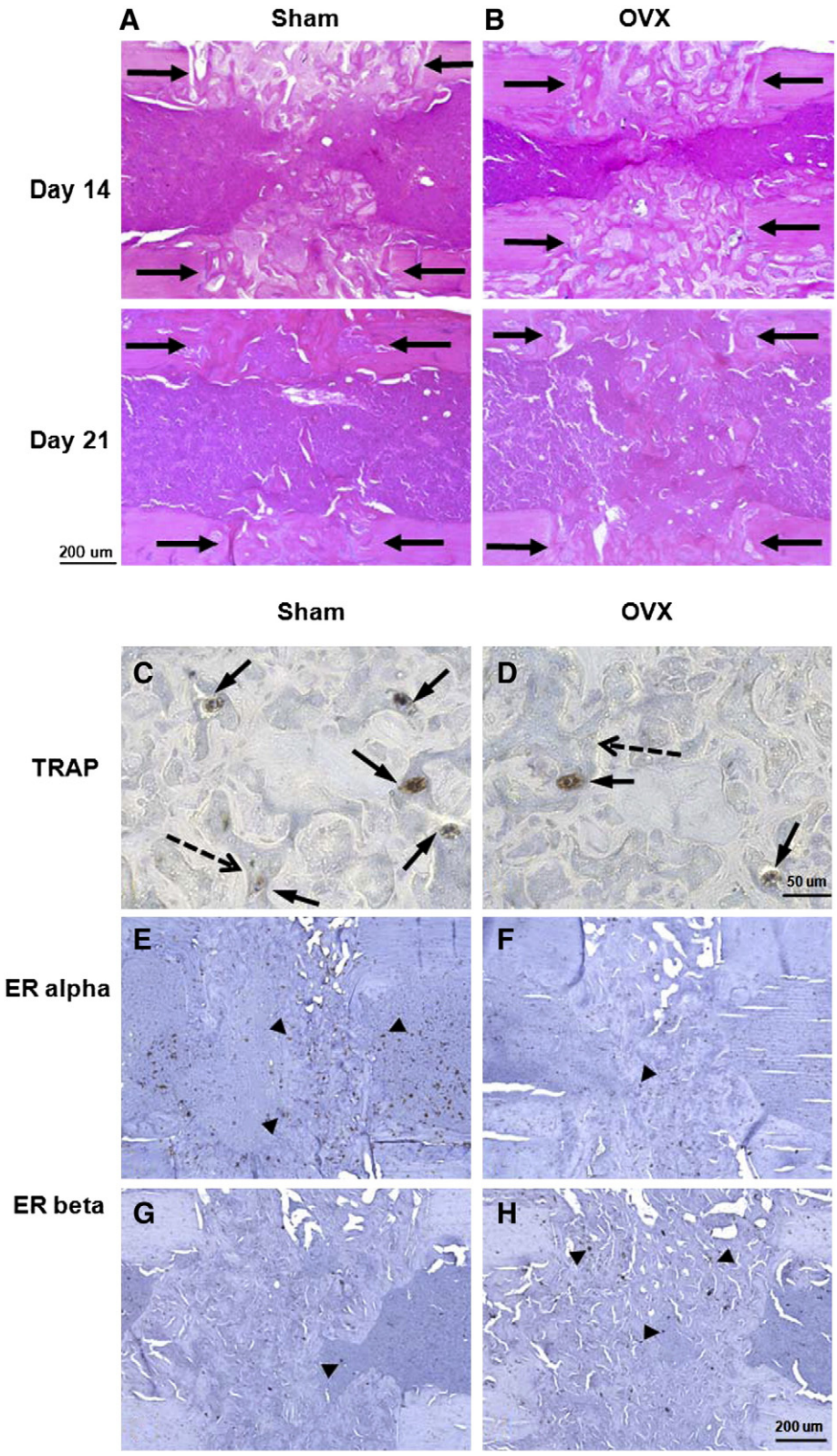

Fig. 4 (*continued*).

growth factor (VEGF), were required for bone formation during bone healing [44,45]. In addition, lower VEGF expression in osteoblasts of OVX animals as compared to Sham animals were also observed previously [46]. Therefore, impaired neovascularization together with impaired bone healing in OVX mice was expected in this study.

Histological examination demonstrated that the OVX mice had less vessel-like structures at day 3 and day 7, which was also supported by less vessel-like structures and poorer network observed in micro-CT-based angiograph at day 7. These results are consistent with a previous study using OVX mice with a femoral shaft fracture

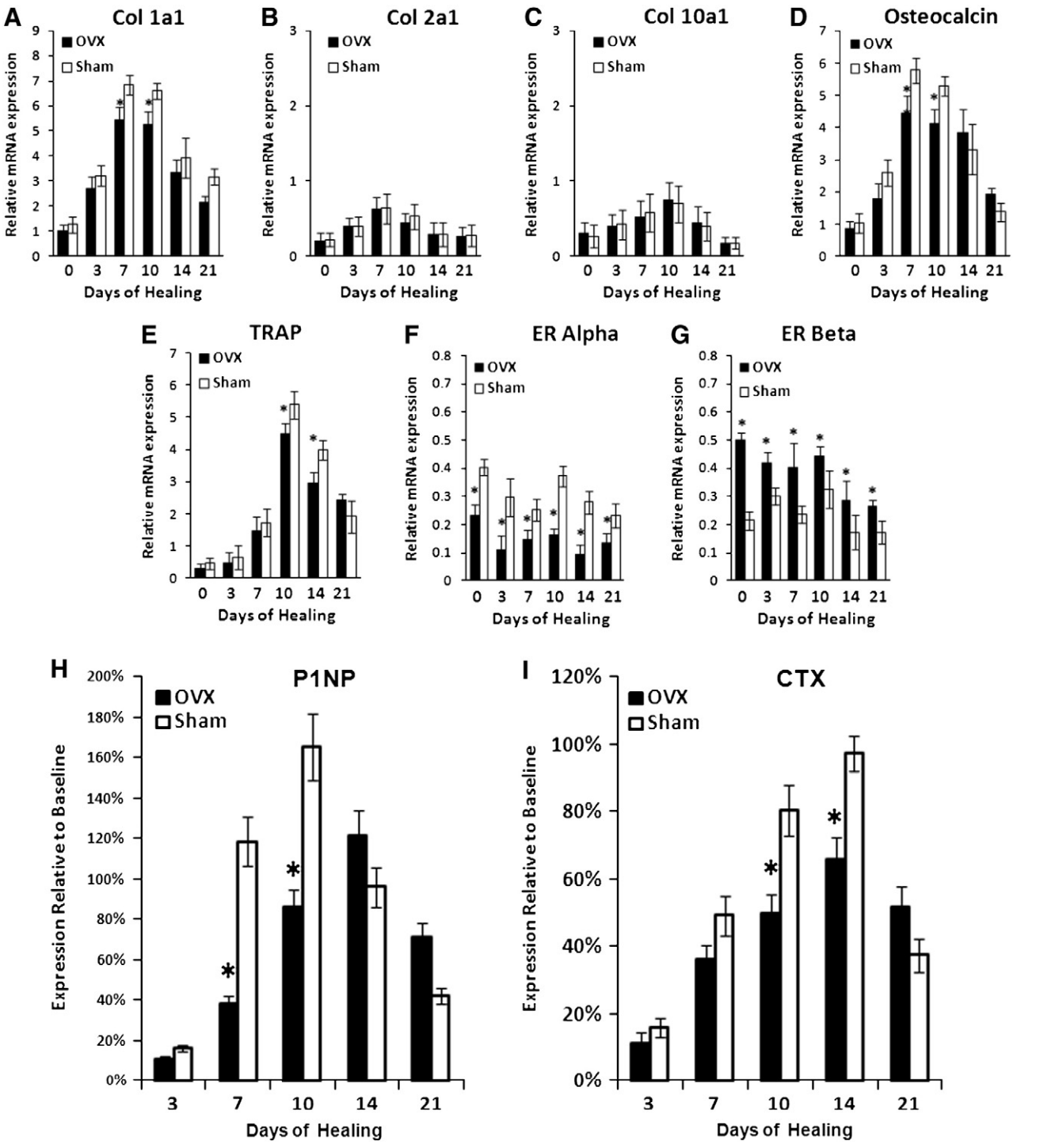

Fig. 5. Temporal analysis of callus gene expression and serum biochemical markers. Temporal changes in Col1a1 (A), Col2a1 (B), Col10a1 (C), osteocalcin, (D) TRAP, (E) ER alpha (F) and ER beta (G) mRNA expression in callus samples following drill-hole surgery were determined by quantitative RT-PCR analysis. Expression levels were normalized to that of β-actin. Concentrations of serum bone formation marker P1NP (H) and serum bone resorption marker CTX (I) were determined by ELISA. Data are reported as means ± SD. N = 4 for mRNA expression, N = 8 for biochemical marker, *: $P<0.05$ between the Sham and OVX groups.

stabilized with external fixation [23], and suggest that impaired neovascularization during osteoporotic bone healing is independent of the fixation. Taken together, our data indicated that neovascularization was impaired during bone healing in the OVX mice as compared to the Sham mice.

Impaired osteogenesis

Micro-CT reconstruction and histological examination consistently demonstrated less new bone formation in both defect region (day 10 and day 14) and intra-medulla region (day 7, day 10 and day 14) in OVX mice as compared to Sham mice, suggesting that intramembranous ossification was impaired during bone healing in the OVX-induced osteoporotic bone. The observed decrease in Col1a1 and osteocalcin mRNA expression and bone formation biomarker P1NP expression in the OVX mice as compared to the Sham mice suggests that activation of osteoprogenitor cells in the OVX mice was impaired. These changes likely contributed to diminished bone formation in the OVX mice during bone healing.

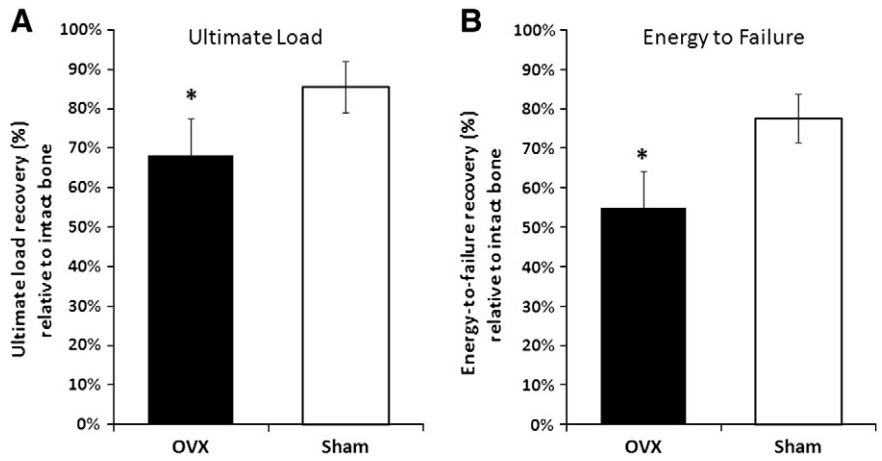

Fig. 6. Mechanical testing of femurs at 21 days post drill-hole injury. Data reflect the average ultimate load (A) or energy-to-failure (B) of the drill-hole femur relative to the contralateral intact femur ± SD. N = 8 for each group, * :$P<0.05$ for comparison between Sham and OVX groups.

Impaired bone remodeling

During the late phase of bone healing, the newly formed bone in the defect region was fully remodeled into a cortical like structure in the Sham mice, whereas remodeling was incomplete in the OVX mice, as evidenced by both micro-CT data and histological examination. The result indicated the remodeling capability from woven bone to lamellar bone was impaired in the OVX mice, consistent with previous reports using an internal or external fixation model [11,12,17]. It could be explained by the significantly higher expression level of bone resorption marker CTX in the Sham mice compared to the OVX mice at day 10 and day 14 after normalization to their corresponding baseline level. In the present study, the use of relative bone resorption level to the baseline was aimed to reflect local bone resorption during bone healing after diminishing the systemic factors. Consistently, the TRAP mRNA expression level from local callus tissue was also significantly higher in the Sham mice compared the OVX mice at day 10 and day 14. Meanwhile, there were more TRAP-positive cells in the Sham mice compared to the OVX mice, which indicated more osteoclast activities. It is known to all that bone resorption is coupled with bone formation in the normal bone physiology. In the present study, the bone formation level from local callus is higher in the Sham mice than the OVX mice. Understandably, the local high bone resorption level in the Sham mice could be predicted.

Low restoration of mechanical properties

The OVX mice had lower restoration capability of mechanical properties than the Sham mice, as evidenced by a lower percent recovery with respect to the ultimate load and the energy-to-failure in OVX mice as compared to Sham mice. The finding is consistent with a previous study using a femoral fracture model with internal fixation [19] and was an obvious consequence of the impaired osteoporotic bone healing processes described above.

Reproducibility of the in vivo micro-CT method for analysis of bone healing

This study is the first to employ *in vivo* micro-CT analysis for longitudinal assessment of bone healing. Micro-CT facilitates monitoring bone structure changes *in vivo*, allows visualization of the healing process, and distinguishes subtle inter-group differences. By eliminating large variations among animals, *in vivo* micro-CT analysis may facilitate reducing sample size with satisfactory statistical significance. The reproducibility tests indicate that the optimal sample size can be determined as follows: $N = 2[(\mu_\alpha + \mu_\beta)S/\delta]^2$ (S is coefficient of variation and δ is percentage difference). The $PE_{\%CV}$ with a 95%CI from all time points and regions was 1.62% to 4.71%, if α was set at 0.05 ($\mu_\alpha = 1.96$), β was set at 10% ($1-\beta = 90\%$, $\mu_\beta = 1.28$) and the percentage difference (δ) = 10%; N would be equal to 2 to 5, whereas the sample size used in the internal or external fixation model was usually 6 to 10 [23,24]. Moreover, the smallest ICC from all time points and regions remained above 0.9, which is very close to perfect reproducibility. More important, the animals should be sacrificed at each time point to obtain the temporal and spatial information when using internal or external fixation model, whereas it did not when using bone drill-hole defect model with *in vivo* micro-CT technique. It would save more animals. Like the advantages presented in other studies using *in vivo* micro-CT [47,48], the technique in combination with drill-hole defect model has great potential to accurately, reproducibly, reliably, and rapidly investigate the bone healing process in mice.

Dysregulated expression of estrogen receptors and bone healing in OVX mice

In the present study, ER alpha mRNA expression in callus tissue was lower in the OVX mice than Sham mice, but ER beta mRNA expression was higher at all time points examined, consistent with our immunohistochemical analysis. It has been reported that decreased ER alpha protein expression and increased ER beta protein expression occurs in the intact bone after ovariectomy in rat [49,50]. Furthermore, up-regulation of ER alpha mRNA and down-regulation of ER beta mRNA has been shown in mesenchymal stem cells obtained from bone marrow of OVX mice treated with estrogen [51]. In general, the dysregulated estrogen receptor expression should be taken into consideration when aberrant biological process is observed after estrogen depletion. Controversial findings from ER alpha complete-null mice have shown that ER alpha either does not affect [52] or stimulate [53] intramembranous and endochondral ossification in female mouse femur. Therefore, the lower expression of ER alpha may not completely explain the impaired healing in the OVX mice. It has been shown that ER beta inhibits angiogenesis in breast cancer cells in vitro using transient transfection assay [54]. On the other hand, a longitudinal ER beta gene knockout study in female mice demonstrated that ER beta signaling inhibits both intramembranous and endochondral ossification during bone development [55,56]. Hence, it is of great importance to explore whether over-expressed ER beta contributes to the altered bone repair observed in the drill-hole defect OVX mouse model in further studies.

Study limitations

It is known that both impaired intramembranous ossification and endochondral ossification occurs in osteoporotic bone. Although the present study provides a model for investigating the functional role of

specific genes or effects of potential therapeutics on impaired intramembranous ossification in osteoporotic bone, the role of dysregulated estrogen receptor expression in this model remains unclear.

Conclusions

This study is the first to employ micro-CT scanning to monitoring *in vivo* bone healing in mice. The bone healing of drill-hole defect in mice with OVX-induced osteoporosis exhibited impaired angiogenesis at early stage, impaired osteogenesis at middle stage and impaired remodeling at late stage, which resulted in compromised mechanical property in the end. The present study thus provides a model to investigate the functional role of specific gene in osteoporotic bone healing and may be useful to develop novel therapeutical strategies.

Acknowledgments

This study was supported by AO Research Grant (S-08-74Z) and CUHK Direct Grant (2008.1.063). The authors declare no conflicts of interest. We also thank Dr. Xie Xin-Hui, Dr. Tang Tao, Dr. Guo Bao-sheng, Dr. Wang Xin-luan and Mr. Wang Yu-Gang for their support in surgery, evaluation and animal care.

Author contributions All authors were involved in drafting the manuscript or revising it critically for important intellectual content, and all authors approved the final version to be published. Dr. Zhang Ge and Dr. Qin Ling have full access to all of the data in the study and take responsibility for the integrity of the data and the accuracy of the data analysis.

- Study conception and design: Qin Ling, Zhang Ge, He Yi-Xin and Pan Xiao-Hua.
- Animal care and surgery: He Yi-Xin, Liu Zhong, Zheng Li-zhen and Pan Xiao-Hua.
- Acquisition of data: He Yi-Xin, Liu Zhong and Zheng Li-zhen.
- Analysis and interpretation of data: Qin Ling, Zhang Ge, He Yi-Xin, Chan Chun-Wai, Lee Kwong-Man and Li Gang.
- Interpretation of data with clinical relevance: Pan Xiao-Hua, Cao Yong-Ping, Leung Kwok-Sui and Hung Leung-Kim.

References

[1] Ferguson C, Alpern E, Miclau T, Helms JA. Does adult fracture repair recapitulate embryonic skeletal formation? Mech Dev 1999;87:57–66.
[2] Einhorn TA. The cell and molecular biology of fracture healing. Clin Orthop Relat Res 1998:S7–S21.
[3] Gerstenfeld LC, Cho TJ, Kon T, Aizawa T, Tsay A, Fitch J, et al. Impaired fracture healing in the absence of TNF-alpha signaling: the role of TNF-alpha in endochondral cartilage resorption. J Bone Miner Res 2003;18:1584–92.
[4] Einhorn TA. The science of fracture healing. J Orthop Trauma 2005;19:S4–6.
[5] Kon T, Cho TJ, Aizawa T, Yamazaki M, Nooh N, Graves D, et al. Expression of osteoprotegerin, receptor activator of NF-kappaB ligand (osteoprotegerin ligand) and related proinflammatory cytokines during fracture healing. J Bone Miner Res 2001;16:1004–14.
[6] Yang X, Ricciardi BF, Hernandez-Soria A, Shi Y, Pleshko Camacho N, Bostrom MP. Callus mineralization and maturation are delayed during fracture healing in interleukin-6 knockout mice. Bone 2007;41:928–36.
[7] Colnot C, Thompson Z, Miclau T, Werb Z, Helms JA. Altered fracture repair in the absence of MMP9. Development 2003;130:4123–33.
[8] Cho TJ, Gerstenfeld LC, Einhorn TA. Differential temporal expression of members of the transforming growth factor beta superfamily during murine fracture healing. J Bone Miner Res 2002;17:513–20.
[9] Kosaki N, Takaishi H, Kamekura S, Kimura T, Okada Y, Minqi L, et al. Impaired bone fracture healing in matrix metalloproteinase-13 deficient mice. Biochem Biophys Res Commun 2007;354:846–51.
[10] Behonick DJ, Xing Z, Lieu S, Buckley JM, Lotz JC, Marcucio RS, et al. Role of matrix metalloproteinase 13 in both endochondral and intramembranous ossification during skeletal regeneration. PLoS ONE 2007;2:e1150.
[11] Hao YJ, Zhang G, Wang YS, Qin L, Hung WY, Leung K, et al. Changes of microstructure and mineralized tissue in the middle and late phase of osteoporotic fracture healing in rats. Bone 2007;41:631–8.
[12] McCann RM, Colleary G, Geddis C, Clarke SA, Jordan GR, Dickson GR, et al. Effect of osteoporosis on bone mineral density and fracture repair in a rat femoral fracture model. J Orthop Res 2008;26:384–93.
[13] Qiao L, Xu KH, Liu HW, Liu HQ. Effects of ovariectomy on fracture healing in female rats. Sichuan Da Xue Xue Bao Yi Xue Ban 2005;36:108–11.
[14] Wang JW, Li W, Xu SW, Yang DS, Wang Y, Lin M, et al. Osteoporosis influences the middle and late periods of fracture healing in a rat osteoporotic model. Chin J Traumatol 2005;8:111–6.
[15] Xu SW, Wang JW, Li W, Wang Y, Zhao GF. Osteoporosis impairs fracture healing of tibia in a rat osteoporotic model. Zhonghua Yi Xue Za Zhi 2004;84:1205–9.
[16] Lill CA, Hesseln J, Schlegel U, Eckhardt C, Goldhahn J, Schneider E. Biomechanical evaluation of healing in a non-critical defect in a large animal model of osteoporosis. J Orthop Res 2003;21:836–42.
[17] Namkung-Matthai H, Appleyard R, Jansen J, Hao Lin J, Maastricht S, Swain M, et al. Osteoporosis influences the early period of fracture healing in a rat osteoporotic model. Bone 2001;28:80–6.
[18] Kim WY, Han CH, Park JI, Kim JY. Failure of intertrochanteric fracture fixation with a dynamic hip screw in relation to pre-operative fracture stability and osteoporosis. Int Orthop 2001;25:360–2.
[19] Meyer Jr RA, Tsahakis PJ, Martin DF, Banks DM, Harrow ME, Kiebzak GM. Age and ovariectomy impair both the normalization of mechanical properties and the accretion of mineral by the fracture callus in rats. J Orthop Res 2001;19:428–35.
[20] Barrios C, Brostrom LA, Stark A, Walheim G. Healing complications after internal fixation of trochanteric hip fractures: the prognostic value of osteoporosis. J Orthop Trauma 1993;7:438–42.
[21] Sodergard J, Sandelin J, Bostman O. Mechanical failures of internal fixation in T and Y fractures of the distal humerus. J Trauma 1992;33:687–90.
[22] Wittenberg RH, Shea M, Swartz DE, Lee KS, White III AA, Hayes WC. Importance of bone mineral density in instrumented spine fusions. Spine 1991;16:647–52.
[23] Ding WG, Zhang ZM, Zhang YH, Jiang SD, Jiang LS, Dai LY. Changes of substance P during fracture healing in ovariectomized mice. Regul Pept 2010;159:28–34.
[24] Egermann M, Heil P, Tami A, Ito K, Janicki P, Von Rechenberg B, Hofstetter W, Richards PJ. Influence of defective bone marrow osteogenesis on fracture repair in an experimental model of senile osteoporosis. J Orthop Res 2010;28:798–804.
[25] Stromsoe K. Fracture fixation problems in osteoporosis. Injury 2004;35:107–13.
[26] Monfoulet L, Rabier B, Chassande O, Fricain JC. Drilled hole defects in mouse femur as models of intramembranous cortical and cancellous bone regeneration. Calcif Tissue Int 2010;86:72–81.
[27] Corrales LA, Morshed S, Bhandari M, Miclau III T. Variability in the assessment of fracture-healing in orthopaedic trauma studies. J Bone Joint Surg Am 2008;90:1862–8.
[28] Uusitalo H, Rantakokko J, Ahonen M, Jamsa T, Tuukkanen J, KaHari V, et al. A metaphyseal defect model of the femur for studies of murine bone healing. Bone 2001;28:423–9.
[29] Cui Q, Xiao Z, Li X, Saleh KJ, Balian G. Use of genetically engineered bone-marrow stem cells to treat femoral defects: an experimental study. J Bone Joint Surg Am 2006;88(Suppl 3):167–72.
[30] Nagashima M, Sakai A, Uchida S, Tanaka S, Tanaka M, Nakamura T. Bisphosphonate (YM529) delays the repair of cortical bone defect after drill-hole injury by reducing terminal differentiation of osteoblasts in the mouse femur. Bone 2005;36:502–11.
[31] Campbell TM, Wong WT, Mackie EJ. Establishment of a model of cortical bone repair in mice. Calcif Tissue Int 2003;73:49–55.
[32] Songlin P, Ge Z, Yixin H, Xinluan W, Pingchung L, Kwoksui L, et al. Epimedium-derived flavonoids promote osteoblastogenesis and suppress adipogenesis in bone marrow stromal cells while exerting an anabolic effect on osteoporotic bone. Bone 2009;45:534–44.
[33] Zhang G, Qin L, Hung WY, Shi YY, Leung PC, Yeung HY, et al. Flavonoids derived from herbal Epimedium brevicornum Maxim prevent OVX-induced osteoporosis in rats independent of its enhancement in intestinal calcium absorption. Bone 2006;38:818–25.
[34] Zhang G, Sheng H, He YX, Xie XH, Wang YX, Lee KM, et al. Continuous occurrence of both insufficient neovascularization and elevated vascular permeability in rabbit proximal femur during inadequate repair of steroid-associated osteonecrotic lesions. Arthritis Rheum 2009;60:2966–77.
[35] Duvall CL, Taylor WR, Weiss D, Wojtowicz AM, Guldberg RE. Impaired angiogenesis, early callus formation, and late stage remodeling in fracture healing of osteopontin-deficient mice. J Bone Miner Res 2007;22:286–97.
[36] Wang W, Hayami T, Kapila S. Female hormone receptors are differentially expressed in mouse fibrocartilages. Osteoarthritis Cartilage 2009;17:646–54.
[37] Yang SH, Liu R, Perez EJ, Wen Y, Stevens Jr SM, Valencia T, et al. Mitochondrial localization of estrogen receptor beta. Proc Natl Acad Sci USA 2004;101:4130–5.
[38] Rauner M, Stupphann D, Haas M, Fert I, Glatigny S, Sipos W, et al. The HLA-B27 transgenic rat, a model of spondyloarthritis, has decreased bone mineral density and increased RANKL to osteoprotegerin mRNA ratio. J Rheumatol 2009;36:120–6.
[39] Gluer CC, Blake G, Lu Y, Blunt BA, Jergas M, Genant HK. Accurate assessment of precision errors: how to measure the reproducibility of bone densitometry techniques. Osteoporos Int 1995;5:262–70.
[40] Shrout PE, Fleiss JL. Intraclass correlations: uses in assessing rater reliability. Psychol Bull 1979;86:420–8.
[41] Schindeler A, McDonald MM, Bokko P, Little DG. Bone remodeling during fracture repair: the cellular picture. Semin Cell Dev Biol 2008;19:459–66.
[42] Komatsu DE, Brune KA, Liu H, Schmidt AL, Han B, Zeng QQ, et al. Longitudinal in vivo analysis of the region-specific efficacy of parathyroid hormone in a rat cortical defect model. Endocrinology 2009;150:1570–9.
[43] Monfoulet L, Malaval L, Aubin JE, Rittling SR, Gadeau AP, Fricain JC, et al. Bone sialoprotein, but not osteopontin, deficiency impairs the mineralization of regenerating bone during cortical defect healing. Bone 2010;46:447–52.
[44] Wohl GR, Towler DA, Silva MJ. Stress fracture healing: fatigue loading of the rat ulna induces upregulation in expression of osteogenic and angiogenic genes that mimic the intramembranous portion of fracture repair. Bone 2009;44:320–30.

[45] Jacobsen KA, Al-Aql ZS, Wan C, Fitch JL, Stapleton SN, Mason ZD, et al. Bone formation during distraction osteogenesis is dependent on both VEGFR1 and VEGFR2 signaling. J Bone Miner Res 2008;23:596–609.
[46] Pufe T, Claassen H, Scholz-Ahrens KE, Varoga D, Drescher W, Franke AT, et al. Influence of estradiol on vascular endothelial growth factor expression in bone: a study in Gottingen miniature pigs and human osteoblasts. Calcif Tissue Int 2007;80:184–91.
[47] David V, Laroche N, Boudignon B, Lafage-Proust MH, Alexandre C, Ruegsegger P, et al. Noninvasive in vivo monitoring of bone architecture alterations in hindlimb-unloaded female rats using novel three-dimensional microcomputed tomography. J Bone Miner Res 2003;18:1622–31.
[48] Buie HR, Moore CP, Boyd SK. Postpubertal architectural developmental patterns differ between the L3 vertebra and proximal tibia in three inbred strains of mice. J Bone Miner Res 2008;23:2048–59.
[49] Zaman G, Jessop HL, Muzylak M, De Souza RL, Pitsillides AA, Price JS, et al. Osteocytes use estrogen receptor alpha to respond to strain but their ERalpha content is regulated by estrogen. J Bone Miner Res 2006;21:1297–306.
[50] Hou NN, Zhu YM, Huang HF. The expression of estrogen receptor alpha and beta in the intervention of different estrogens in rat bone metabolism. Fen Zi Xi Bao Sheng Wu Xue Bao 2006;39:289–96.
[51] Zhou S, Zilberman Y, Wassermann K, Bain SD, Sadovsky Y, Gazit D. Estrogen modulates estrogen receptor alpha and beta expression, osteogenic activity, and apoptosis in mesenchymal stem cells (MSCs) of osteoporotic mice. J Cell Biochem Suppl 2001;Suppl. 36:144–55.
[52] Tozum TF, Oppenlander ME, Koh-Paige AJ, Robins DM, McCauley LK. Effects of sex steroid receptor specificity in the regulation of skeletal metabolism. Calcif Tissue Int 2004;75:60–70.
[53] Chagin AS, Lindberg MK, Andersson N, Moverare S, Gustafsson JA, Savendahl L, et al. Estrogen receptor-beta inhibits skeletal growth and has the capacity to mediate growth plate fusion in female mice. J Bone Miner Res 2004;19:72–7.
[54] Hartman J, Lindberg K, Morani A, Inzunza J, Strom A, Gustafsson JA. Estrogen receptor beta inhibits angiogenesis and growth of T47D breast cancer xenografts. Cancer Res 2006;66:11207–13.
[55] Ke HZ. In vivo characterization of skeletal phenotype of genetically modified mice. J Bone Miner Metab 2005;23(Suppl):84–9.
[56] Ke HZ, Brown TA, Qi H, Crawford DT, Simmons HA, Petersen DN, et al. The role of estrogen receptor-beta, in the early age-related bone gain and later age-related bone loss in female mice. J Musculoskelet Neuronal Interact 2002;2:479–88.